

Image-Based Size Analysis of Agglomerated and Partially Sintered Particles via Convolutional Neural Networks

M. Frei*, F. E. Kruis

*Institute of Technology for Nanostructures (NST) and Center for Nanointegration Duisburg-Essen (CENIDE)
University of Duisburg-Essen, Duisburg, D-47057, Germany*

Abstract

There is a high demand for fully automated methods for the analysis of primary particle size distributions of agglomerated, sintered or occluded primary particles, due to their impact on material properties. Therefore, a novel, deep learning-based, method for the detection of such primary particles was proposed and tested, which renders a manual tuning of analysis parameters unnecessary.

As a specialty, the training of the utilized convolutional neural networks was carried out using only synthetic images, thereby avoiding the laborious task of manual annotation and increasing the ground truth quality. Nevertheless, the proposed method performs excellent on real world samples of sintered silica nanoparticles with various sintering degrees and varying image conditions.

In a direct comparison, the proposed method clearly outperforms two state-of-the-art methods for automated image-based particle size analysis (Hough transformation and the ImageJ ParticleSizer plug-in), thereby attaining human-like performance.

Keywords: imaging particle size analysis, agglomerate, convolutional neural network (CNN), Mask R-CNN, Hough transformation, ImageJ ParticleSizer

1. Introduction

Powders play an important role in chemical industry. In Europe, approximately 60 % of the products of this branch of industry are powders themselves and another 20 % of the products require powders during their production [1]. Accordingly, particle measurement technologies, e.g. for the determination of particle size distributions (PSDs), are of vital importance for the chemical industry.

The distinction of objects on images and the image background, a process referred to as image segmentation, is an important requirement for imaging particle analysis techniques. The simplest way to do so is to create a binary image, where black pixels represent the image background, while white pixels represent the sought-after objects. Subsequently, the sizes of the objects can be attained by determining the numbers of pixels of connected white regions. It is plain to see that overlapping or occluded objects, for instance caused by agglomeration, are a major source of error for this approach, because they impede the detection of the individual objects. This is a severe problem, because the detection of overlapping and occluded objects plays an important role in many applications, such as the determination of the primary PSD of agglomerated particles on microscopic images [2] as well as bubbles in multi-phase reactors [3] or the detection and characterization of fibers [4].

Often, the solutions for such problems are either highly customized and thus difficult to reuse and adapt or extremely laborious (e.g. manual analysis) and therefore expensive.

While humans are very good at recognizing overlapping objects as individual objects, this task is usually much harder for algorithms, because they lack the flexibility to adapt to the specific image conditions. Therefore, we propose the utilization of artificial neural networks (ANNs) and more specifically a convolutional neural network (CNN), we named DeepParticleNet (DPN), which can autonomously learn to detect individual objects based on a large number (usually a few dozens or hundreds) of already annotated images via supervised learning. In case of a necessary adaption to new imaging conditions it suffices to adjust the training data and to retrain the DPN.

The fact that the DPN heavily depends on training data is one of its major advantages, because it minimizes the amount of a priori knowledge which is necessary to achieve a reliable object detection. However, at the same time, it is also its largest disadvantage because already evaluated training data is often not available and has to be created manually, which is a very laborious task. Therefore, we propose the synthesis of the images and ground truths needed for the training. Prior to the image synthesis, the characteristics of real images are analyzed and used to yield lifelike synthetic images with known ground truths, thereby making a manual annotation of images obsolete. A certain degree of realism of the synthesized images is very important to guarantee a realistic training of the DPN. Otherwise, the application to real images might yield insufficient results.

The combination of a self-learning method and a customized synthesis of its training data allow a high degree of specialization, while still maintaining high levels of adaptability and robustness.

*Corresponding author. Tel.: +49 203 379-3621
Email address: max.frei@uni-due.de (M. Frei)

1.1. Automated Image-Based Particle Sizing Methods

In the context of this work, it is sensible to categorize established and innovative methods for the determination of the PSDs of agglomerated and occluded particles into three groups: conventional, ANN-based and CNN-based methods.

Conventional Methods. Conventional methods utilize classic image processing techniques for the identification of the individual primary particles. Among the most popular of these methods are the watershed transformation (WST) [5–7], ultimate erosion (UE) [8, 9] and the Hough transformation (HT) [10–13]. WST- and UE-based methods are usually fast and feature a small memory footprint. However, they often tend to over-segment images, due to their noise susceptibility. In contrast, HT-based methods are considerably slower and consume much more memory. In return, they are more robust towards noise and other image distortions. One major disadvantage that conventional methods share is the fact that they usually feature one or more parameters, which need to be set by the user according to the imaging conditions, to achieve a high precision. Therefore, a change in the imaging conditions, e.g. due to an operator change, may result in faulty analysis results and the necessity to retune the parameters.

ANN-based Methods. In contrast to conventional methods, ANN-based methods [14–16] can help to avoid image specific parameters. They are therefore usually fully automatic and more robust to changes of the imaging conditions. However, they often use shape descriptors as inputs, which have to be identified and implemented during the design of the ANNs. Apart from the increased design-effort, the use of shape descriptors also leads to a severe loss of information. While, on the one hand, this reduction is necessary to make the use of ANNs feasible in the first place, it can also severely impede the detection accuracy.

CNN-based Methods. The main advantage of CNNs for image-based particle analysis is the fact that, unlike ANNs, they can not only be trained on feature interpretation but also feature extraction. CNNs-based methods are therefore often referred to as end-to-end methods. They take the raw data, i.e. images, as input and output the sought-after measurands [17]. Current CNN-based particle analysis methods focus either on the shape-discrimination of particles, e.g. agglomerate/non-agglomerate [18] or on the identification and subsequent PSD measurement of single particles [19]. In contrast, within this publication, a method for the CNN-based PSD measurement of agglomerated and even partially sintered primary particles will be presented.

2. Theory of Convolutional Neural Networks

The proposed method is based on CNNs, which are a special form of ANNs. Therefore, the fundamental principles of CNNs shall be explained briefly within the following sections. For a comprehensive introduction to ANNs and CNNs, please refer to Kriesel [20] and Goodfellow et al. [17], respectively. Additionally, a very sophisticated CNN architecture, the Mask R-CNN, which was first introduced by He et al. [21], will be elaborated upon, as it is the basis for the proposed method.

2.1. Convolutional Neural Networks

CNNs introduce a new kind of layer to ANNs: The eponymous convolutional layer, which uses a convolution as activation function and matrices (also referred to as filter kernels) as weights. These properties make CNNs very effective for image processing, because they can learn complicated image filtering sequences to solve a given task by adjusting their filter kernels during the training [17].

Image filtering, i.e. convolving an image with a filter to extract a feature map, is a standard procedure in conventional image processing. However, usually, the utilized filters have to be engineered manually for a certain application (e.g. edge detection) [22]. This optimization can be automated very effectively using CNNs. Another advantage of CNNs is the fact that they learn multiple filters per layer and combine very simple filters (e.g. for oriented edges) of lower layers to filters of increasing complexity in higher layers. Therefore, they can extract very complicated features (e.g. letters or faces) [23]. Due to this strategy, CNNs usually apply a drastically increased number of layers in comparison to conventional ANNs, which inspired the term deep learning [24].

2.2. Mask R-CNN

The Mask R-CNN [21] architecture is a very sophisticated example of a CNN, which consists of six components (see Figure 1).

Feature Extraction Network (Backbone). The feature extraction network, also referred to as backbone, of a Mask R-CNN is a CNN, used to extract prominent features over the entirety of an input image. One advantage of the Mask R-CNN architecture is the fact that the backbone is easily interchangeable, which substantially facilitates transfer learning¹.

Region Proposal Network. The region proposal network (RPN) is a CNN that proposes bounding boxes of regions of interest (ROI), by evaluating the feature map, which was output by the feature extraction network preceding the RPN. Subsequently, the extracted regions of the feature map are used for all tasks involved in the instance segmentation, i.e. the segmentation, classification and bounding box regression of each instance, after the extracted regions have been refined by ROI alignment. The fact that a single feature map is used for all tasks of the instance segmentation greatly improves the training and inference speed of the Mask R-CNN architecture.

Region of Interest Alignment. The resolution of the feature map is usually significantly smaller than the one of the input image, due to one or more downsampling steps in the backbone. Masks generated based on the low resolution features can therefore be misaligned with the objects on the input image. This issue was

¹Transfer learning means that, at the beginning of the training, the weights of an ANN are not initialized randomly but with weights that resulted from a training on a different task (e.g. the classification of everyday objects). Like that, knowledge gathered during the training on one task is transferred to another task.

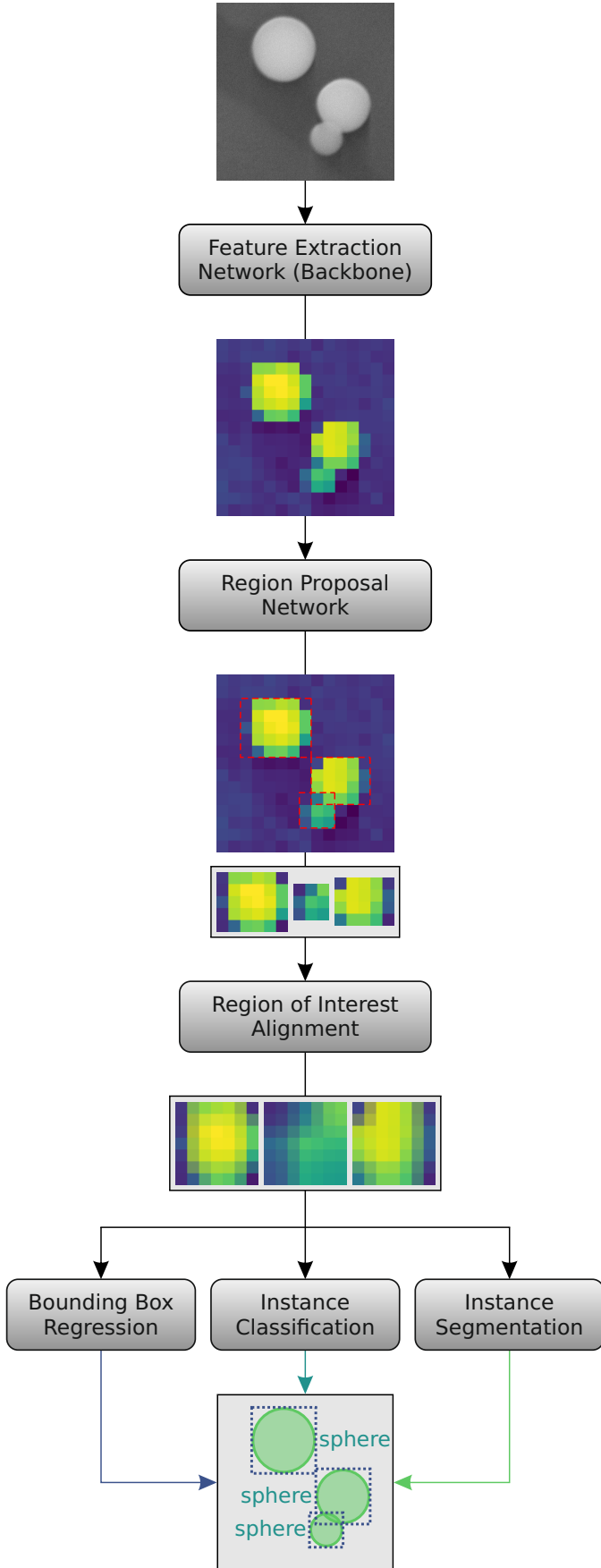


Figure 1: Mask R-CNN structure (inspired by [25]).

fixed by the authors of the Mask R-CNN architecture by introducing ROI alignment. This means that before the extraction of the ROI, the feature map is bilinearly interpolated to improve the alignment of the utilized ROI of the feature map with the actual objects on the input image.

Bounding Box Regression Block. The bounding boxes of the proposed ROI usually do not fit the objects on the original image perfectly. Therefore, a small ANN consisting of fully-connected layers is used for the regression of the bounding boxes, based on the previously extracted feature map, thereby improving their accuracy.

Instance Classification Block. In the instance classification block, each instance is classified, again using a small ANN of fully-connected layers with the respective ROI of the feature map as input.

Instance Segmentation Block. The segmentation of the instances featured in the ROI is realized by performing a pixel-based binary classification, based on the previously extracted feature map, with help of a small CNN. During the classification, each pixel is assigned one of the classes *object* or *background*.

3. Method

The workflow of the proposed method, where the Mask R-CNN is applied to synthetic and real particle images, consists of two phases: the training and the application phase.

Training Phase. During the training phase (see Figure 2), real images – e.g. scanning electron microscopy (SEM) or transmission electron microscopy (TEM) images – are surveyed for their characteristic properties (e.g. imaging method, particle shape, agglomerate size, noise and blur levels, contrast, etc.). Optionally, these observations can be supplemented with a priori knowledge about the sample at hand (e.g. approximate range of the geometric mean diameter and geometric standard deviation), to specialize the DPN during the training and yield better analysis results in the application phase. The gathered information is used to set the parameters of the image synthesis, after which the synthetic images are used for the training of the DPN. After the DPN has been trained on the synthetic images, it is tested based on a small set of already evaluated real images, to prove that it can be applied to new and therefore unknown samples in the application phase.

Application Phase. During the application phase (see Figure 3), the DPN outputs three kinds of information for each detected primary particle: a bounding box, a mask and a class. These attributes allow the determination of a huge variety of properties of the particle ensemble, e.g. PSD, fractal structure, degree of sintering, mixture composition and many more.

While the training of the DPN usually takes a longer time (in the range of hours) and requires one or more graphics processing units (GPUs), the application to images can be done on a central processing unit (CPU) within seconds (see Section 4.4).

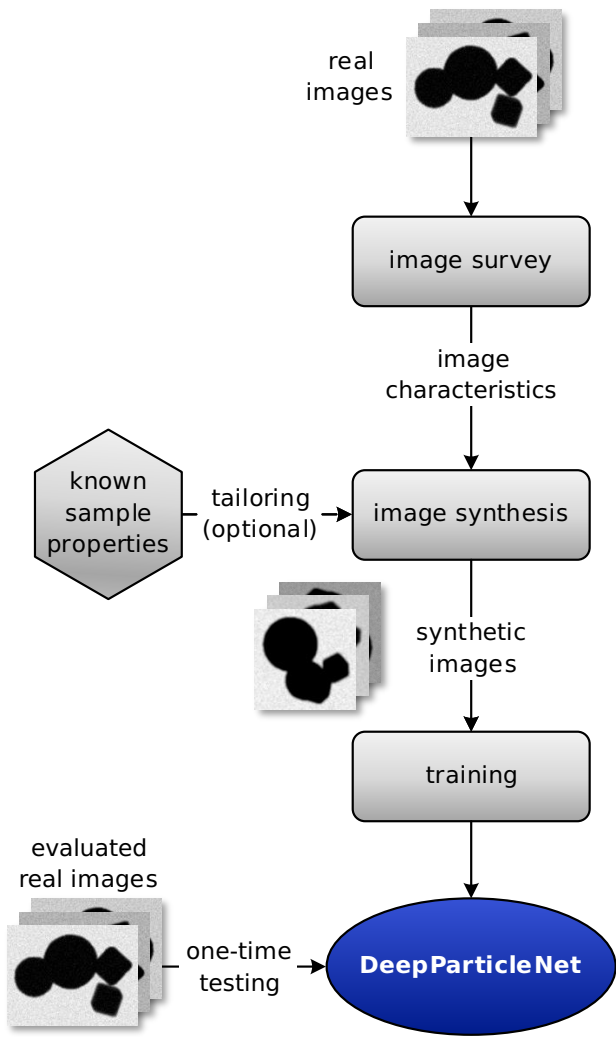


Figure 2: Workflow of the DPN training phase.

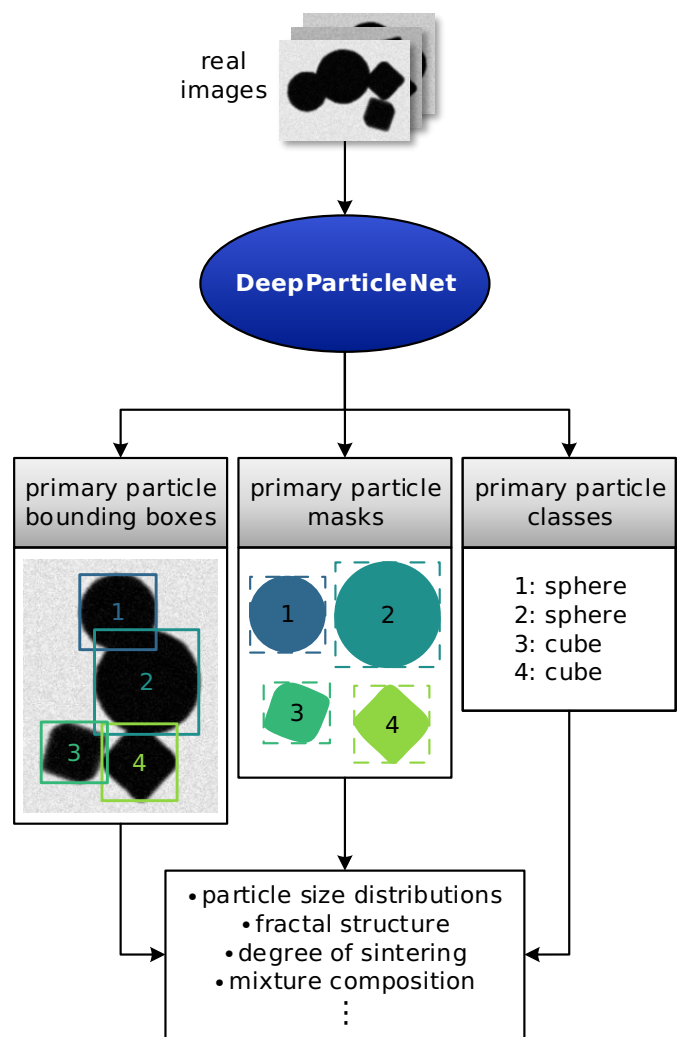


Figure 3: Workflow of the DPN application phase.

3.1. Training, Validation and Test Data

For the training of an ANN, usually three kinds of data sets are needed: a training set, a validation set, to verify that the ANN is not being overfit during the training and a test set, to check the generalization abilities of the ANN on previously unseen data after the training. For the proposed method, the training set as well as the validation set are synthetically generated to avoid the laborious manual annotation of the large number of images needed for the training and validation. However, for the test set, it is essential to use real images, to prove that the ANN is able to make correct predictions for the data, which the ANN is actually going to be used on. For the publication at hand, SEM images were used for the testing of the proposed method. However, also images from TEM or other imaging methods could be used.

Training and Validation Data – Image Synthesis. A key feature of the proposed method is the fact that only synthetic images are used for the training of the DPN, so that there is no need for a laborious manual evaluation of real images, to get a ground truth, which is essential for supervised learning.

The image synthesis is a three step process (see Figure 4):

- **Meshing:** During the meshing², the three-dimensional geometry of a set of particles is generated. The shape of the resulting mesh depends on a variety of primary particle parameters, such as their primitive shape and their PSD, as well as agglomerate properties, such as the agglomerate size distribution, the degree of sintering and the agglomeration mode. It is noteworthy that it is not the goal of the meshing to emulate the physical formation but rather the visual appearance of particles and agglomerates.
- **Rendering:** The rendering process transfers the mesh into a set of pixel-based intensity maps. Each of these maps represents an image feature, such as color, diffuseness or shadowing. Analogously to the meshing, the rendering does not try to simulate the image formation on a physical basis, but rather aims at a life-like emulation of the resulting image.
- **Compositing:** For the compositing, a weighted sum of the previously rendered intensity maps is calculated to form an intermediate image. Subsequently, characteristic image distortions such as blur and noise are added to the image, to increase its life-likeness.

Apart from the reduced effort, a key advantage of the image synthesis is the perfect knowledge about otherwise unknown features of the training data, such as the three-dimensional agglomerate geometry. This knowledge can then be used to improve the quality of the ground truth and thereby the training of the DPN. In the studies at hand, the quality of the ground truth was improved drastically by the incorporation of occlusion (see

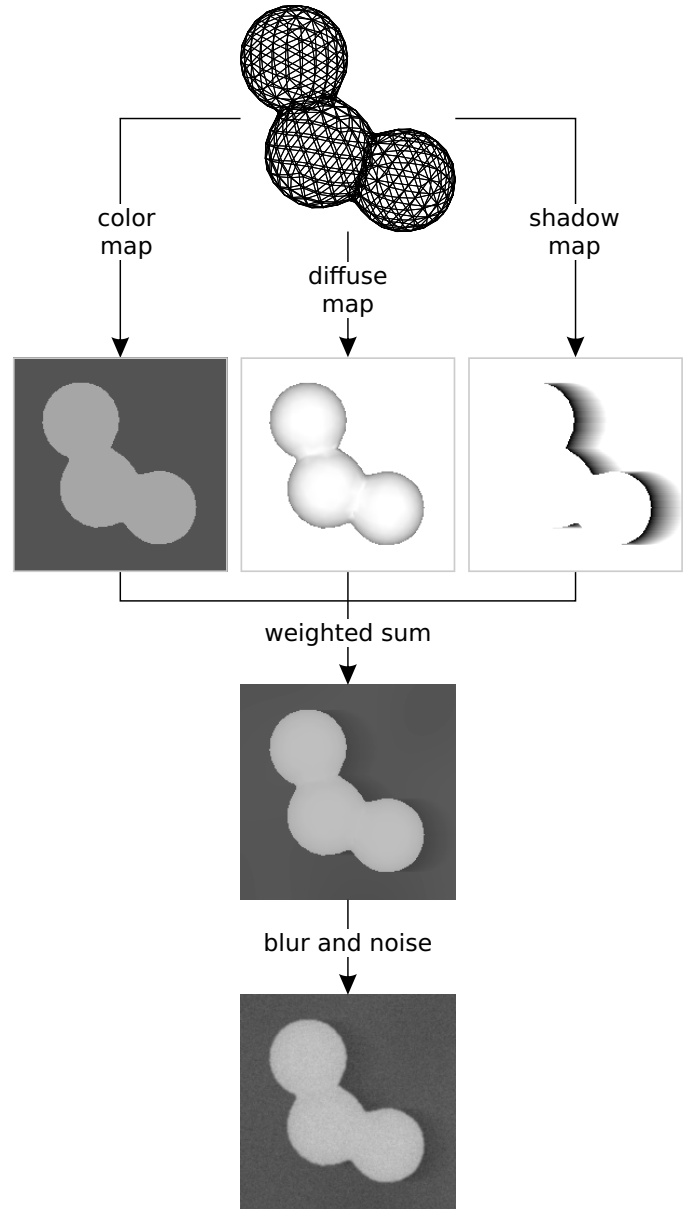


Figure 4: Elementary steps of the image synthesis.

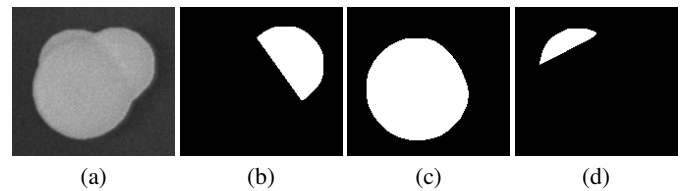


Figure 4: Synthetic image of an agglomerate (a) and associated ground truth, i.e. convex occlusion masks of the primary particles (b-d).

Figure 4), a very important phenomenon for nontransparent materials, which is often ignored during manual evaluations.

To facilitate the large scale image synthesis, a toolbox – the synthetic particle image creator (synthPIC)³ – was especially implemented. With help of the synthPIC toolbox, a mixture of synthetic SEM images, with varying degrees of sintering as well as agglomerate and primary particle sizes was generated (see Figure 5a), to mimic the diversity of the real SEM images of the test set (see Figure 5b).

Test Data – Scanning Electron Microscopy. As test data, real SEM images of agglomerated and partially sintered silica nanoparticles were used (see Figure 5b). The images resulted from a sintering study, performed by Babick et al. [26].

During the sintering study, particles of a certain size were generated and subsequently sintered at different temperatures in the range of 1000 to 1500 °C (see Supplementary Materials Table SM.1). As a result, 10 samples which exhibit increasing degrees of sintering were produced and subsequently analyzed with SEM⁴. For the samples with sintering temperatures in the range of 1000 to 1300 °C and 1350 to 1500 °C magnifications of 100 k× and 50 k× were used respectively, due to the primary particle size increasing with the sintering temperature. In total, the test data consists of 10 data sets, with a total of 99 images (see Supplementary Materials Table SM.2), featuring 6126 primary particles in 699 agglomerates (according to a manual evaluation). Each image has a resolution of 768×1024 px.

A very important feature of the test data is its high level of heterogeneity with respect to the image conditions (e.g. brightness, contrast, noise, blur and background texture), due to varying sample and instrument conditions as well as varying SEM operators. Usually these factors severely impede the reliability of imaging particle size analysis methods. Therefore, good results on heterogeneous test data would indicate a high robustness and flexibility of the proposed method.

Similarity of Training and Test Data. There are two levels of similarity with respect to the training and the test data: On the one hand, there is the visual likeness of the synthetic and real images and on the other hand, there is the possible similarity of the distributions of the target measurand, i.e. the primary particle size of the depicted particles.

Concerning the two kinds of possible similarity of the utilized training and test data, we face a dilemma. The synthesized images must exhibit a certain life-likeness, so that the DPN can pick up characteristic features of the training data, which also apply to the test data. This includes, at least to a certain extent, also the primary particle sizes. However, the training and test data may not be too similar, so that the DPN learns to generalize and does not suffer from a data bias.

To study the similarities of the training set and the 10 test sets with regard to the measurand, the primary PSD P of the

training set was compared to the primary PSDs Q_i of the test sets (see Figure 6). As equivalent diameter, the maximum Feret diameter⁵ $\max(d_{\text{Feret}})$ of the primary particle masks was used, to account for the occlusions in case of the training set (see paragraph *Training and Validation Data – Image Synthesis*).

The comparison yielded two important qualitative insights:

- The PSD of the training set covers the full range of all individual test set PSDs and is therefore much broader.
- The similarity of the training set PSD and the individual test set PSDs is rather low.

For a better, quantitative, comparability of the similarities of the PSDs of the training and the test sets, it is helpful to introduce a similarity or inversely a divergence measure. A common measure for the divergence of two probability distributions P and Q_i is the Kullback-Leibler divergence [27]:

$$D_{\text{KL}}(P \parallel Q_i) = \sum_x P(x) \log \left(\frac{P(x)}{Q_i(x)} \right), \quad (1)$$

where, for the case at hand, P and Q_i are the primary PSDs of the training set and one of the test sets respectively.⁶ The Kullback-Leibler divergence yields values which range from 0 for identical to 1 for completely different probability distributions.

The comparisons of the PSDs of the training with the test sets yield Kullback-Leibler divergences in the range from 0.432 to 0.870 (see Supplementary Materials Table SM.3), which indicate low levels of similarity. It can therefore be concluded that the risk of a data bias is low.

3.2. DeepParticleNet

The DPN is the CNN at the core of the proposed method, which is trained on the detection of individual primary particles. Its architecture was inspired by the Mask R-CNN architecture, developed by He et al. [21] and based on an implementation of Abdulla [28], realized with Keras [29] and TensorFlow [30], controlled by Python [31].

3.2.1. Architecture

As backbone for the DPN, a ResNet architecture [32] was chosen, because it offers several benefits for the task at hand: Firstly, it allows the use of very deep networks, without facing problems concerning vanishing gradients, i.e. that the training stagnates, due to the involved gradients becoming very small [32]. Secondly, the ResNet architecture offers high accuracies at comparably low computational costs [33]. Thirdly, there are multiple variants of the ResNet architecture with increasing numbers of layers, which allows a choice between higher accuracies and lower computational costs. Last but not least, due to

²In computer graphics, a mesh is a collection of triangles in a three-dimensional space, which form the surface of an object.

³The synthPIC toolbox will be made available on the following website in the near future: <https://github.com/maxfrei750/synthPIC4Matlab>

⁴JEOL JSM-7500F Field Emission Scanning Electron Microscope

⁵The Feret diameter d_{Feret} of a non-circular object depends on the direction of the measurement. Therefore, the maximum Feret diameter is the maximum of all the Feret diameters of an object. It equals the largest possible euclidean distance of two points on the outline of an object.

⁶For the calculation, bins where either $P(d) = 0$ or $Q_i(d) = 0$ were excluded.

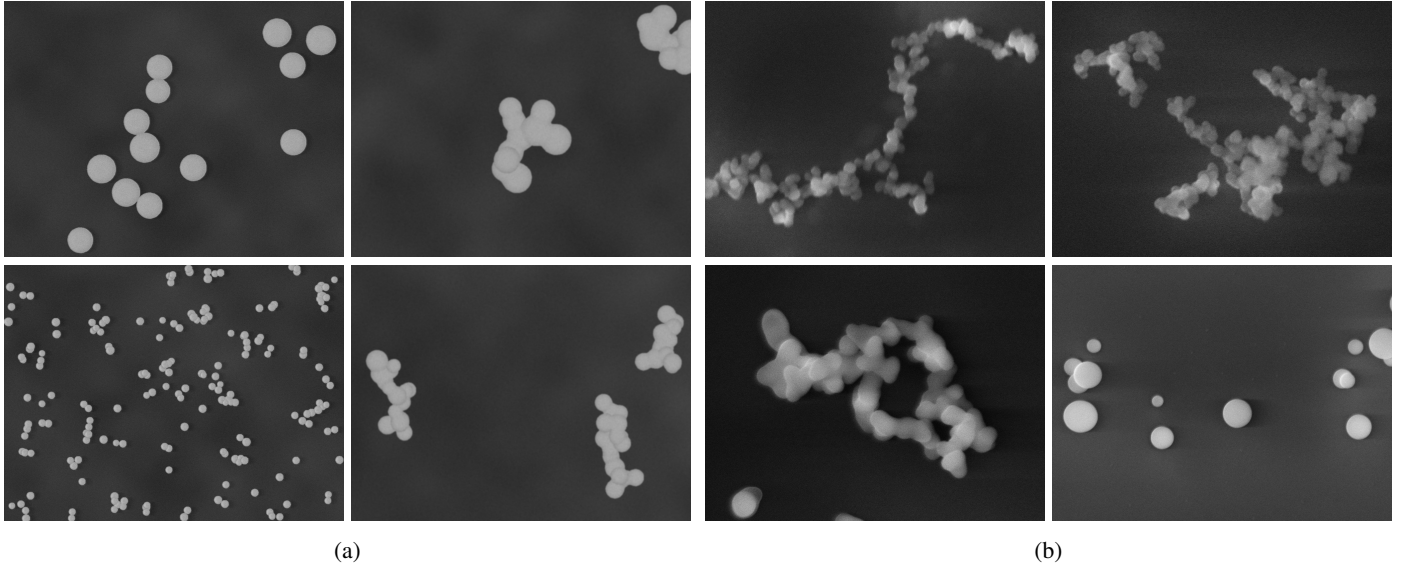


Figure 5: Examples of synthetic images used for the training and validation (a) and real images from the 10 data sets used for the testing (b) of the DPN. For a complete overview of the 10 test sets please refer to the Supplementary Materials (Figure SM.1).

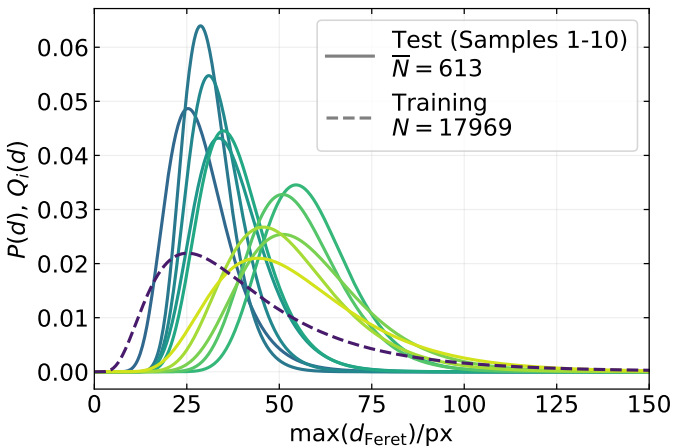


Figure 6: Comparison of the distributions P and Q_i of the maximum Feret diameter $\max(d_{\text{Feret}})$ of the primary particles of the training set and the 10 test sets, respectively. N is the number of primary particles.

its popularity, there are numerous sets of weights available for the various ResNet models, which result from extensive trainings on large data sets of everyday objects (e.g. ImageNet [34] and common objects in context (COCO) [35]) and can therefore be used for transfer learning.

Choice of a ResNet Variant as Backbone. As mentioned before, there are multiple variants of the ResNet architecture (see Figure 7). The top-1-accuracy⁷ of the models, when being trained on the ImageNet data set, increases with an increasing number of layers. However, this also increases their computational

⁷The top-1-accuracy is a common measure for classification tasks (such as the ImageNet competition). It is calculated as the percentage of correctly classified images, under the condition that the method is only allowed to make a single prediction per image.

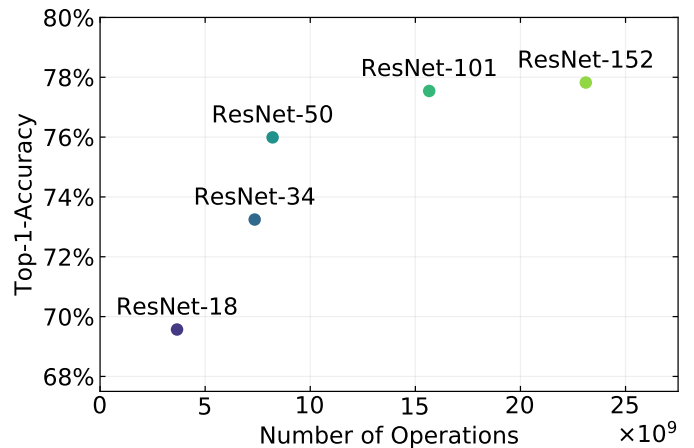


Figure 7: Top-1-accuracies of different ResNet variants, when being trained on the ImageNet data set, versus their computational costs, i.e. the number of operations, needed for a single forward pass (data from [32], inspired by [33]).

costs. For the proposed method, ResNet-50 and ResNet-101 were chosen as possible candidates for the backbone of the DPN, due to their high accuracies at reasonable computational costs.

For the final decision concerning the backbone of the DPN, the losses $\mathcal{L}_{\text{validation}}$ of the two candidate models on the validation data set were compared (training conditions: see Supplementary Materials Table SM.4; see also Section 3.2.2). On the one hand for randomly initialized weights and on the other hand for initializations with weights resulting from previous trainings on the ImageNet and the COCO data set (see Figure 8).

The comparison yielded three important insights:

- Transfer learning is a very effective means to yield lower validation losses.
- Weights resulting from a previous training on the COCO

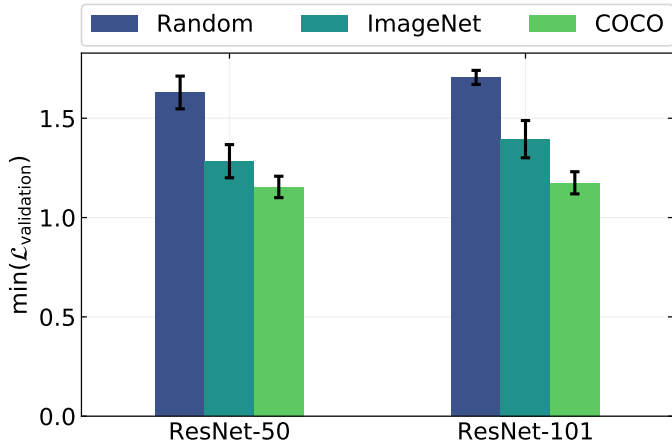


Figure 8: Comparison of the minimum validation losses $\mathcal{L}_{\text{validation}}$ of DPNs on the validation data set, with ResNet-50 and -101 models, initialized with different weights, as backbones (3 repetitions, error bars represent $\pm\sigma$).

data set yield lower validation losses than weights resulting from a previous training on the ImageNet data set.

- DPNs with ResNet-50 backbones offer slightly lower minimum validation losses, compared to DPNs with ResNet-101 backbones. However, the differences are negligible.

The last of the three insights is rather counterintuitive, considering the higher performance of the ResNet-101 backbone on the ImageNet data set (see Figure 7). However, a possible explanation might be the fact that the additional layers of the ResNet-101 backbone extract increasingly intricate image features. While this might be beneficial for the classification of very complex objects like animals, it might be superfluous for the detection of rather simple objects like primary particles, which mainly consist of basal features like straight and curved edges. Therefore, additional layers might rather increase the noise than extract helpful image features.

Ultimately, the ResNet-50 model initialized with weights resulting from a previous training on the COCO data set was used as backbone for the DPN, due to it exhibiting the highest performance at the lowest computational cost.

3.2.2. Training

From an application-oriented point of view, the training of ANNs is the most elaborate task for the application of deep learning methods to new problems. An architecture that is in principle suitable for the solution of a given task, might yield insufficient results, when being applied to new kinds of data. Therefore, this section will present state-of-the-art concepts and strategies for the training of ANNs, as a guide line, to enable the reader to apply the proposed method to his or her own data.

Early Stopping. Early stopping is a very simple, yet effective regularization method, i.e. a means to avoid overfitting [17]. During the training of ANNs, it is a very common phenomenon that the validation loss reaches a minimum while the training loss still decreases. Therefore, by stopping the training early, i.e. as soon as the validation loss starts to increase again, we

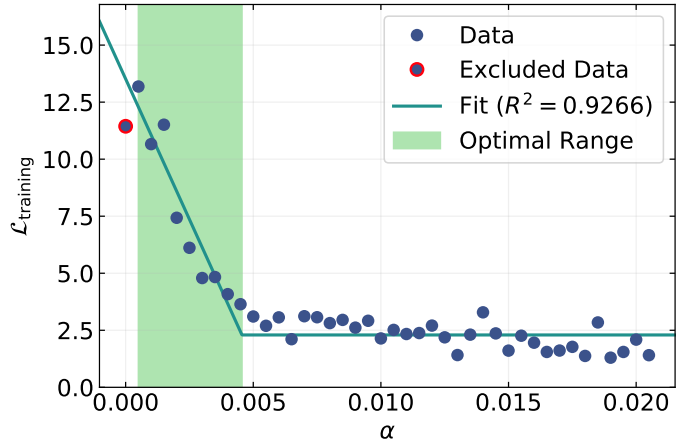


Figure 9: Learning rate range test – Training loss $\mathcal{L}_{\text{training}}$ versus the learning rate α .

can not only save on training time but also reach a higher level of generalization and thus a better performance during the deployment of the ANN. However, due to the noisy nature of the validation loss, especially for the small batch sizes⁸ often used in deep learning, it is sensible not to stop the training immediately when encountering a potentially merely local minimum of the validation loss. Instead, it is sensible to wait for a predefined number of epochs, to ensure that the validation loss really does not decrease any further. The number of epochs to be waited is called early stopping patience. For the publication at hand, multiple early stopping patiences were tested (see Supplementary Materials Figure SM.2 and Table SM.5) and an early stopping patience of 10 epochs was used, as a compromise between training time and minimum validation loss.

Optimization of the Learning Rate. The learning rate α is the most important hyperparameter for the training of CNNs [36]. Often, the optimal value for the learning rate is determined by rather brute force, using grid or random search. However, these simple approaches are very time consuming. Therefore, for the proposed method, a cyclical learning rate strategy was tested, as described by Smith [36], using code of Kenstler [37]. This means that during the training, the learning rate was not held constant but varied cyclically within an optimal learning rate range.

According to Smith [36], a simple test can be utilized to find the optimal learning rate range. The learning rate is linearly increased and the training loss of the trained CNN is monitored. The optimal learning rate ranges from α_{min} , the point of the initial training loss maximum, to α_{max} , where the training loss no longer decreases (see Figure 9).

To introduce a reproducible measure for α_{max} , the data from the learning rate range test was fit with a function of the form

$$f(\alpha) = \max(m\alpha + b, c) \quad (2)$$

⁸The batch size is the number of samples (in the case at hand images) that is processed simultaneously by an ANN. It is therefore a very important hyperparameter to control the memory consumption.

where data points with learning rates below α_{\min} were excluded from the fit. Subsequently, the crossover of the two line segments of $f(\alpha)$ at

$$\alpha_{\max} = \frac{c - b}{m} \quad (3)$$

was used as upper boundary α_{\max} of the optimal learning rate range.

Using the learning rate range determined in this way and the recommendation of Smith [36] concerning the optimal cycle length (see Supplementary Materials Table SM.6), a training utilizing a cyclical learning rate policy was carried out. The resulting minimum validation loss was compared to that achieved using a random learning rate search (see Supplementary Materials Figure SM.3) and the default learning rate (0.001, according to [28]), respectively (see Figure 10).

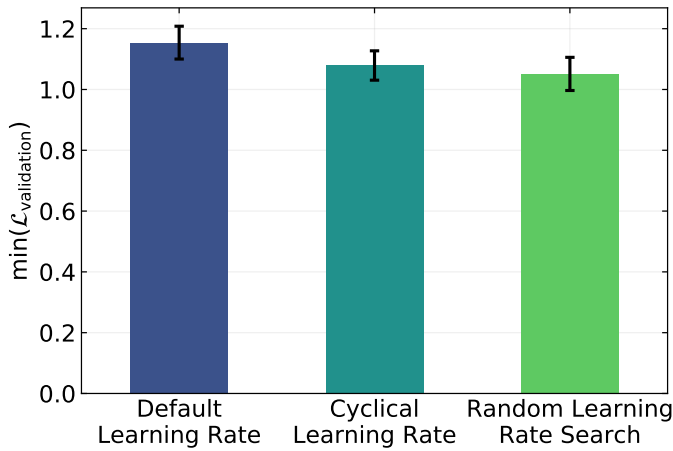


Figure 10: Comparison of minimum validation losses $\mathcal{L}_{\text{validation}}$ achieved with different learning rate optimization strategies (3 repetitions, error bars represent $\pm\sigma$).

The comparison shows that the default learning rate does not yield optimal results. Both the cyclical learning rate strategy as well as the random learning rate search can improve the minimum validation loss, with the latter performing slightly better. However, the random learning rate search consumes a substantially larger amount of training time and is very susceptible to small changes concerning the randomly chosen learning rate (see Supplementary Materials Figure Sm.3). Therefore, the cyclical learning rate strategy was utilized for the further experiments.

Optimal Number of Training Images. The fact that the proposed method utilizes synthetic images for the training of the DPN allows us to be very generous with respect to the number of utilized training images. However, if the training was to be performed on real images, e.g. to further improve the performance of the proposed method, the training data would have to be annotated manually, which is a very laborious task. Therefore, to give an orientation on how many training images are actually necessary, the influence of the number of training images on the minimum validation loss of the DPN was examined (see Figure 11; training conditions: see Supplementary Materials Table SM.8).

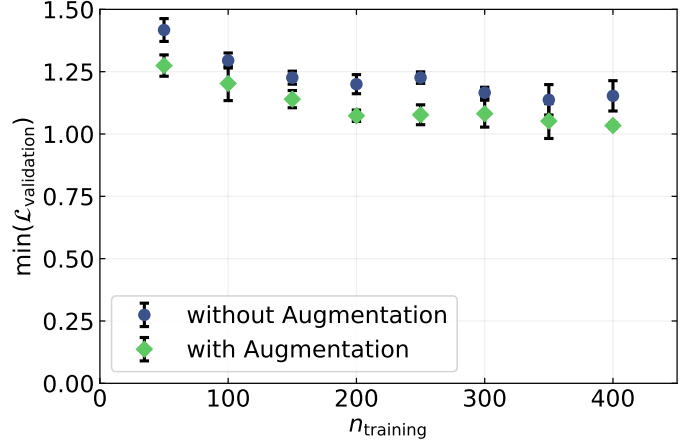


Figure 11: Minimum validation losses $\mathcal{L}_{\text{validation}}$ versus the number of images in the training set n_{training} , with and without image augmentation (3 repetitions, error bars represent $\pm\sigma$).

The minimum validation loss decreases with an increase of the training set size up to a number of 300 images. However, beyond this point additional images do not further improve the performance of the DPN, so that it reaches a validation loss threshold.

Image Augmentation. A probate means to decrease the necessary number of training images is image augmentation, i.e. that training images are being reused after they have been transformed (e.g. rotated) or distorted (e.g. blurred). Like that, the number of training images can effectively be increased and the generalization capabilities of the model are enhanced, due to the training being more versatile [17].

For an evaluation of the potential benefits of image augmentation for the given use case, the influence of the number of training images on the minimum validation loss of the DPN was reexamined, using a selection of up to two, from a list of five, image augmentations (see Appendix Table A.3; training conditions: see Supplementary Materials Table SM.9).

The results of the investigation (see Figure 11) clearly show that image augmentation can reduce the required number of training images. If image augmentation is used, the original validation loss threshold of the DPN (at 300 training images) is already reached at 150 training images and the new validation loss threshold is encountered already at 200 images and is approximately 8% lower. Therefore, image augmentation was used for all further experiments.

Final Training. The final DPN, which was used to generate the results presented in Section 4, was designed and trained based on the insights of Section 3.2. However, the early stopping patience was increased to 20, to further improve the minimum validation loss of the model. Additionally, three training runs were carried out and the model featuring the absolute minimum validation loss ($\mathcal{L}_{\text{validation}} = 0.955$) was selected. Overall, the minimum validation loss was reduced by approximately 46%,



Figure 11: Area A (a) and convex area A_{convex} (b) of an agglomerate.

in comparison to the worst-case scenario⁹, by careful choice of the backbone and the application of the training strategies presented within this section.

4. Results

To assess the eligibility of the proposed method for image-based particle size measurements, the final DPN¹⁰ (training conditions: see Appendix Table A.4) was tested on 10 different test sets, consisting of real SEM images (see Section 3.1). In the process, the detection quality, the accuracy of the PSD measurement as well as the analysis speed was surveyed. Additionally, the performance of the proposed method was compared to those of two prominent, already established methods – the MATLAB version of the HT [38] and the ImageJ ParticleSizer (PS) plug-in [39, 40] – in the aforementioned disciplines.

The non-default parameters of the HT and the ImageJ PS that were used during the comparison are given in the Supplementary Materials, Tables SM.11 and SM.12, respectively.

4.1. Solidity as a Measure for the Sintering Degree

The main difference between the 10 test samples is their increasing sintering degree. Therefore, it is necessary to quantify the sintering degree to study its influence on the performance of the three tested methods. For this purpose, the solidity S was utilized as an easily obtainable measure for the sintering degree. It is defined as the ratio of the area A , i.e. the number of pixels, of an object to the area of its convex hull A_{convex} (see Figure 11) [41]:

$$S = \frac{A}{A_{\text{convex}}} \quad (4)$$

Figure 12 depicts the mean solidities of the agglomerates of the 10 test sets versus the respective sintering temperatures. As expected, the solidity increases with rising temperatures until it cannot increase any further because all primary particles are already sintered.

⁹ResNet-101 backbone with randomly initialized weights, constant default learning rate, 400 training samples and no image augmentation (see Figure 8).

¹⁰The source code of the specific version of the DPN toolbox, the final model and the training, validation and test data sets, used for the training of the DPN as well as the generation of the results presented in this section are available via the following link:

<https://github.com/maxfrei750/DeepParticleNet/releases/v1.0>

Additionally, the training, validation and test data sets are part of the BigParticle.Cloud (<https://bigparticle.cloud>).

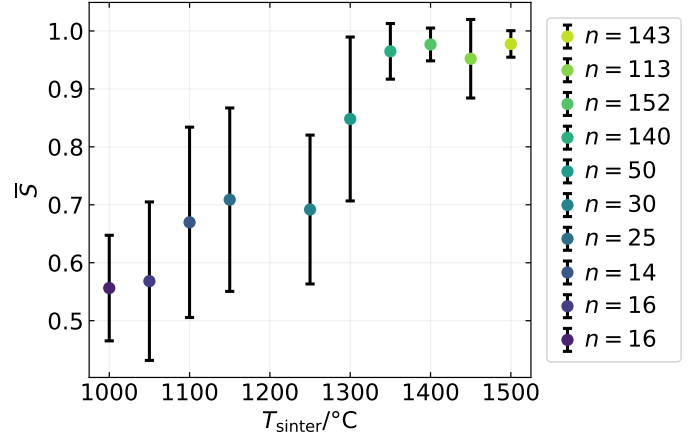


Figure 12: Mean solidities \bar{S} of the agglomerates of the samples of the test set versus the respective sintering temperatures T_{sinter} . n is the number of dates, i.e. the number of agglomerates in the respective sample, used for the calculation of the mean value. Error bars represent $\pm\sigma$.

4.2. Detection

For some applications, e.g. structure analysis, not only the reliable detection of the primary particle sizes but also of their position is elemental. Therefore, the detection quality of the proposed method was assessed both qualitatively and quantitatively.

4.2.1. Qualitative Evaluation

Figure 13 depicts a comparison of original images from the 10 test sets and the corresponding detections by the proposed method, the HT and the ImageJ PS. Although a comparison based on images can only be qualitative, there are already some important insights to be gained.

Human Perspective. Even as a human, it is difficult to decide where individual primary particles begin and end. This applies especially to the samples 1 to 7, which feature a lot of sintering necks. Therefore, there is a very important insight, to keep in mind for the later comparison of the tested methods, when the manual evaluation is used as a reference: For some samples, there is no such thing as a definitive ground truth.

Proposed Method. The proposed method marks only the visible parts of primary particles and yields very plausible results for all the samples. A few primary particles that feature a strong blur or a very low contrast are omitted by the analysis. The detected primary particles feature a medium to high amount of circularity, which is plausible, considering the nature of the sintering process.

Hough Transformation. The HT omits many primary particles when being confronted with rather fractal agglomerates (see samples 1 to 6). Due to the underlying measuring principle, it only yields perfectly circular detections, which often feature a high degree of overlap.

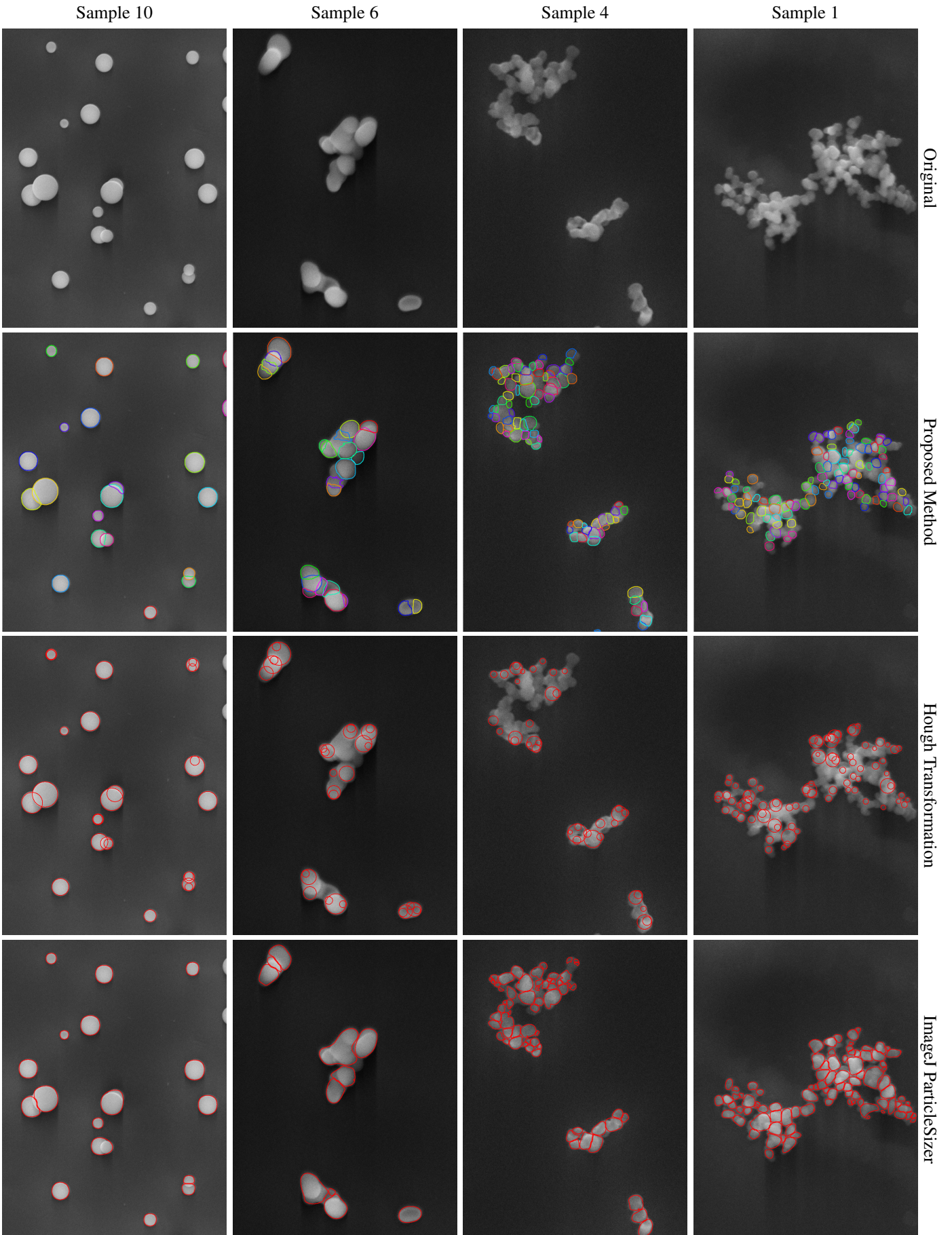


Figure 13: Comparison of randomly picked original images and the corresponding detections of the proposed method, the HT and the ImageJ PS from 4 of the 10 test sets. For a complete overview of the 10 test sets please refer to the Supplementary Materials (Figure SM.5).

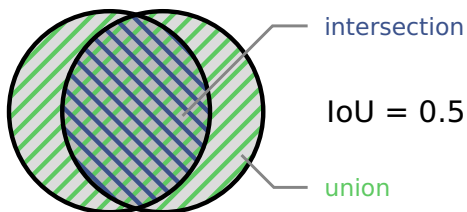


Figure 14: Illustration of the intersection over union metric.

ParticleSizer. The most apparent difference of the detections of the ImageJ PS to those of the other two tested methods is the fact that particles touching the border of the image are ignored during the analysis. Unfortunately, this feature cannot be disabled in the options. Apart from that, the ImageJ PS plausibly fills the area of the agglomerates with detections and exhibits very few omissions and no overlap. However, the detections are often quite bulky, non-circular and concave, which is implausible, considering the nature of the sintering process.

Intermediate Result. All three methods offer a reliable detection of primary particles for the samples 8 to 10, which are already highly sintered and therefore very circular. For the samples 1 to 7, based on the first impression, the proposed method seems to offer the most reliable, intuitive and physically plausible detection, followed by the ImageJ PS and the HT. Due to the fact that these impressions can only be qualitative, the detection quality will be quantified within the next section.

4.2.2. Quantitative evaluation

A common metric for the detection quality is the average precision, which is basically the percentage of correct detections. The criterion, whether a detection can be considered correct is usually the intersection over union (IoU) of the object to be detected and the predicted detection [35]. As the name implies, the IoU is the ratio of the areas of the intersection and the union of object and prediction (see Figure 14). Therefore, the average precision can be defined at multiple IoU thresholds. Commonly used thresholds are $\text{IoU} = 0.5$ and $\text{IoU} = 0.75$, which yield AP_{50} and AP_{75} , respectively. To lessen the impact of the IoU threshold, the mean of the average precision at multiple IoU thresholds, usually in the stepped range [0.50:0.05:0.95], can be calculated, which is simply referred to as AP [42].

Figure 15 depicts a comparison of the average precisions of the three tested methods for the 10 test samples (for comparisons of the AP_{50} and AP_{75} , please see Supplementary Materials Figure SM.4). As ground truth, the results from a manual analysis were used. The quantitative evaluation of the detection quality confirms the qualitative impressions from the previous section. For all 10 test samples, the proposed method outperforms the other two tested methods. Just as it might be expected, test samples with lower solidities are far more challenging for the tested methods than samples featuring higher solidities.

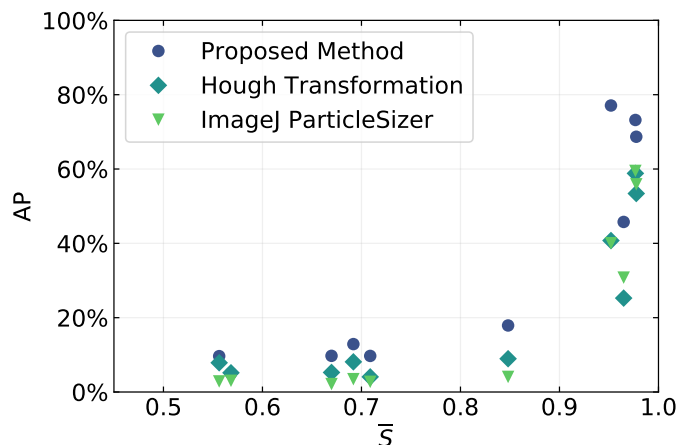


Figure 15: Average precisions AP retrieved via the proposed method, the HT and the ImageJ PS versus the mean solidities \bar{S} of the 10 test samples.

4.3. Primary Particle Size Distribution Measurement

Depending on the application, the capability of the three tested methods to correctly reproduce the underlying primary PSDs of the test samples is more important than the perfect detection of every primary particle. Therefore, the primary PSDs, as measured by each of the three methods were compared to the manually determined primary PSD, for each of the 10 test samples (see Supplementary Materials Figure SM.6).

As equivalent diameter, the maximum Feret diameter was used as a compromise between the perfectly circular detections of the manual analysis and the HT on the one hand and the irregularly shaped detections of the proposed method and the ImageJ PS on the other hand.

Proposed Method. The PSDs retrieved via the proposed method agree very well with the manually determined PSDs for all the samples except for sample 6. However, this sample is very challenging for the HT and the ImageJ PS as well. Of the three tested methods, the proposed method still shows the highest agreement with the manual analysis results.

Hough Transformation. The HT is clearly biased towards a primary particle size of approximately 25 to 30 px, which results in rather strong deviations from the manual analysis. Unfortunately, the reasons for this behavior remain unclear.

ParticleSizer. The ImageJ PS shows a good agreement with the manual analysis for the samples 8 to 10, i.e. samples which mainly feature agglomerates with small numbers of rather circular primary particles. For the other samples, the PSDs retrieved via the ImageJ PS differ from the manually determined PSDs, especially with respect to the geometric standard deviation.

Intermediate Result. The proposed method clearly outperforms the ImageJ PS and the HT. Particularly its consistently high reliability across nearly all the test samples is remarkable.

4.3.1. Accuracy versus Sintering Degree

To survey the impact of the sintering degree on the PSD measurement accuracy of the three tested methods, the geometric mean diameter d_g , the geometric standard deviation σ_g and the primary particle number N were determined for the PSDs of the 10 test samples, retrieved via the three tested methods. Subsequently, the percentage errors $\Delta d_{g,\%}$, $\Delta \sigma_{g,\%}$ and $\Delta N_{\%}$ of these three parameters were determined according to the following equation:

$$\Delta X_{\%,i} = \frac{X_i - T_i}{T_i} \cdot 100\%, \quad (5)$$

where i is the sample index, T_i is the desired value as determined via manual analysis and X_i is the actual value retrieved via one of the tested methods.

Finally, the percentage errors $\Delta d_{g,\%}$, $\Delta \sigma_{g,\%}$ and $\Delta N_{\%}$ of each of the three tested methods for each of the 10 test samples, were plotted versus the corresponding mean solidities \bar{S} (see Figure 16).

Geometric Mean Diameter. The geometric mean diameters determined via the proposed method (see Figure 16a) exhibit only small deviations from the manual analysis (-4 to 13 %), thereby outperforming the HT (-33 to -2 %) and the ImageJ PS (-12 to 20 %) by a large margin. While the errors of the proposed method and the ImageJ PS are symmetrical and mostly independent from the mean solidity, the HT has a tendency to underestimate the geometric mean diameter, especially for samples of high mean solidity.

Geometric Standard Deviation. The percentage errors of the proposed method regarding the geometric standard deviation (-10 to 5 %, see Figure 16b) are similar to those of the geometric mean diameter and thereby again clearly outperform the HT (1 to 25 %) and the ImageJ PS (-2 to 62 %). While the proposed method again exhibits rather symmetrical errors, the ImageJ PS and the HT both have a tendency to overestimate the geometric standard deviation. Furthermore, the impact of the mean solidity is small for the proposed method and the HT but clearly noticeable for the ImageJ PS.

Primary Particle Number. Also with respect to the determination of the number of primary particles (see Figure 16c), the proposed method exhibits smaller errors (-44 to 39 %) than the HT (-49 to 46 %) and the ImageJ PS (-58 to 64 %). In general, the errors of all three tested methods are significantly larger for the determination of the primary particle number, than they are for the determination of the geometric mean diameter and the geometric standard deviation. Independent of the solidity, all three tested methods have a tendency to underestimate the primary particle number, except for the HT, which overestimates the primary particle number for samples of large solidity.

Intermediate Result. The survey of the impact of the solidity on the PSD measurement capabilities of the three tested methods demonstrates that the proposed method clearly outperforms the ImageJ PS as well as the HT and is very robust towards the sintering degree of the analyzed samples.

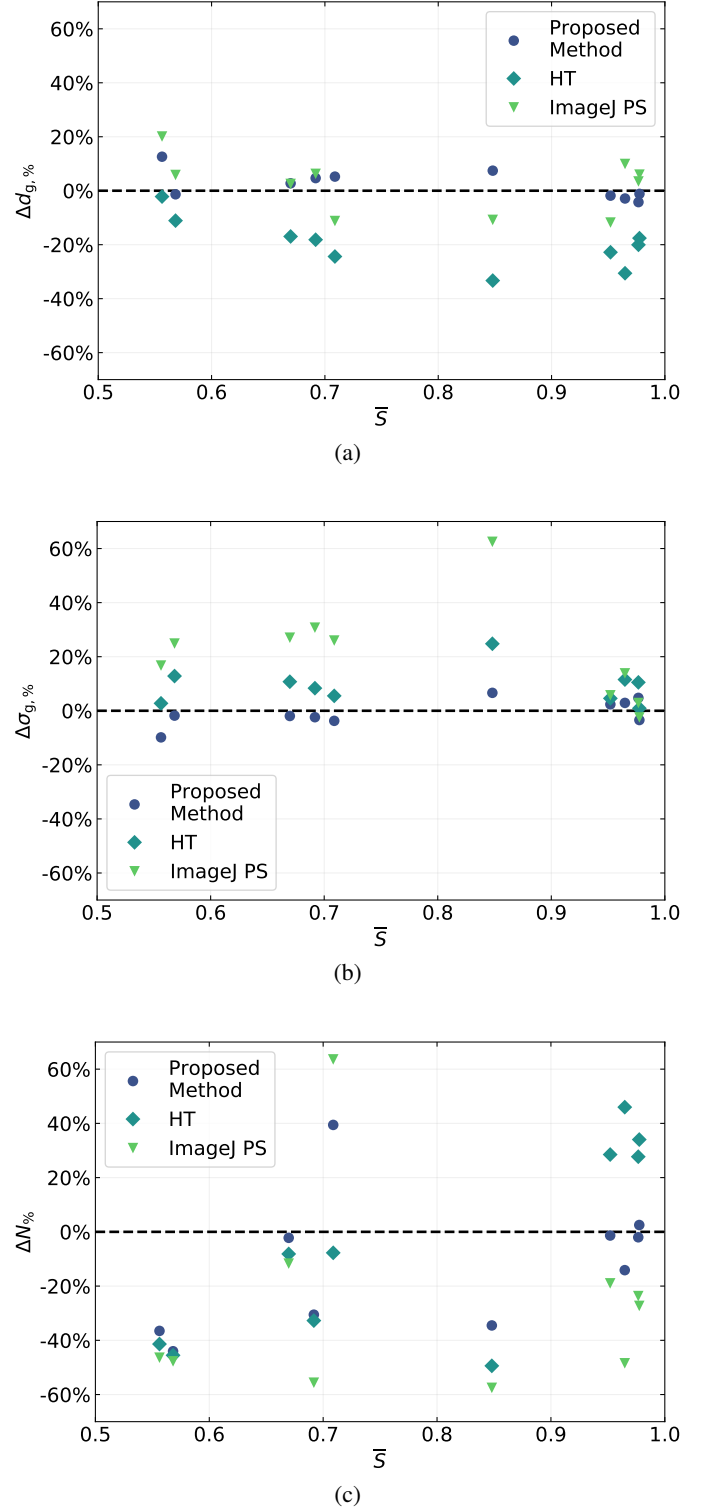


Figure 16: Percentage errors of the geometric mean diameters $\Delta d_{g,\%}$ (a), the geometric standard deviations $\Delta \sigma_{g,\%}$ (b) and the numbers of primary particles $\Delta N_{\%}$ (c) retrieved via the proposed method, the HT and the ImageJ PS versus the mean solidities \bar{S} of the 10 test samples.

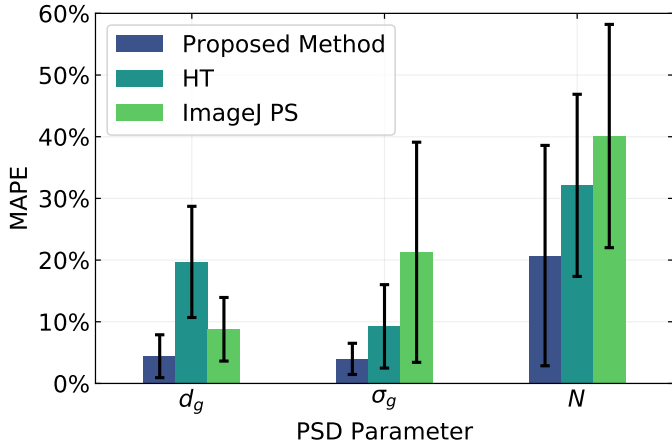


Figure 17: Mean absolute percentage errors MAPE of the PSD parameters d_g , σ_g and N across the 10 test sets, as retrieved via the proposed method, the HT and the ImageJ PS (error bars represent $\pm\sigma$ of the absolute percentage errors).

4.3.2. Overall Accuracy

To allow for a better comparison of the accuracies of the three tested methods, it is useful to describe the error of each method with help of a single characteristic number per sought-after PSD parameter (geometric mean diameter, geometric standard deviation and primary particle number) that gives an intuition of the performance of the tested methods across all 10 test sets. A suitable characteristic number for the given use case is the mean absolute percentage error (MAPE), which is defined as [43]:

$$\text{MAPE} = \frac{1}{n} \cdot \sum_{i=1}^n |\Delta X_{\%,i}|, \quad (6)$$

where i is the sample index and n is the number of dates, i.e. the number of test sets.

Advantageous properties of the MAPE are its easy interpretability and the fact that negative and positive errors do not mutually compensate.

Figure 17 depicts a comparison of the MAPEs of the geometric mean diameter, the geometric standard deviation and the primary particle number, across all 10 test samples for the three tested methods. It can be clearly seen that the proposed method is not only superior to the HT and the ImageJ PS for each of the PSD parameters, but also that it is the only tested method that is capable of a reliable determination of both the geometric mean diameter *and* the geometric standard deviation. It thereby achieves accuracies at a near-human level (approximately 4% error for the geometric mean diameter and 1% error for the geometric standard deviation [14]).

4.4. Analysis Speed

The analysis speed of the tested methods is a very important property, especially for the use in on-line measurement setups. Therefore, the analysis speed was surveyed by a tenfold measurement of the analysis times of each of the tested methods for each of the 10 test sets. Subsequently, the analysis speeds of the tested methods were calculated, on the one hand based on the number of images and on the other hand based on the number

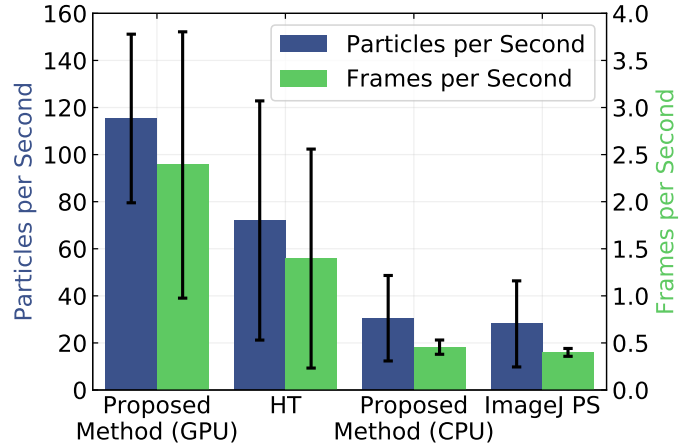


Figure 18: Analysis speeds of the proposed method, the HT and the ImageJ PS, on the one hand based on the number of analyzed images and on the other hand based on the number of analyzed particles (10 repetitions for each of the 10 test sets, error bars represent $\pm\sigma$).

of primary particles in the respective test sets. Ultimately, the mean and the standard deviation of all measurements of each method were calculated and compared (see Figure 18). As a specialty, the analysis speed of the proposed methods was measured twice, once when being run on the CPU and once when being run on a single GPU.¹¹

Both, the analysis speed measurement based on the number of images as well as the analysis speed measurement based on the number of primary particles yield very similar results (see Figure 18). The proposed method clearly outperforms the other tested methods when being run on a GPU, the reason for its dominance being its extremely high degree of parallelism. When being run on a CPU, the proposed method is still slightly faster than the ImageJ PS. However, on a CPU, both methods are clearly outperformed by the HT. As expected, all of the tested automated methods outspeed human operators (0.5 to 0.1 particles per second) by a large margin.

5. Conclusion and Outlook

Within this work, a novel, deep learning-based, method for the pixel-perfect detection and sizing of agglomerated, aggregated or occluded primary particles was proposed and validated. Therefore, the very powerful Mask R-CNN architecture was carefully adapted to and trained on SEM images of nanoparticles, using state-of-the-art training strategies, such as early stopping, transfer learning, a cyclical learning rate schedule and image augmentation.

As a specialty, the training was carried out using only synthetic SEM images, which were produced by the especially implemented synthPIC toolbox, to avoid the laborious task of manual annotation and to increase the quality of the ground truth. Despite the training on synthetic images, the proposed method performed excellent on real world samples, belonging

¹¹For the specifications of the test system, please refer to Appendix Tables A.1 and A.2.

to 10 test sets, which resulted from a sintering study of silica nanoparticles and exhibited various sintering degrees and image characteristics, due to varying SEM operators as well as changing sample and instrument conditions.

To evaluate the performance of the proposed method, it was compared to two established methods for the determination of primary PSDs, the HT and the ImageJ PS plug-in. The proposed method clearly outperformed both of the other tested methods, exhibiting a MAPE as low as 4 % across all test sets, for both the geometric mean diameter and the geometric standard deviation. It thereby attains human-like performance and reliability.

Also the analysis speed of the proposed method was compared to those of the HT and the ImageJ PS. Once again, the proposed method clearly outperformed the other tested methods by a large margin, as long as it was run on a GPU. However, it might not be fast enough for some image-based on-line measurement applications. Fortunately, the speed of the method can be increased nearly linearly by using multiple GPUs in parallel. Nevertheless, future studies will concentrate on achieving higher analysis speeds. Last but not least, the development of unsupervised deep learning strategies for the reliable and fast measurement of PSDs are of utmost interest, because they would lift the requirement of a known ground truth and thereby the necessity of manual annotation or image synthesis.

Acknowledgment

The authors gratefully acknowledge the support via the project "20226 N – Deep Learning Particle Detection" of the DECHEMA e.V. research foundation, which was funded by the German Federation of Industrial Research Associations (AiF) within the program for Industrial Corporate Research (IGF) of the Federal Ministry for Economic Affairs and Energy (BMWi) on the basis of a decision by the German Bundestag. All authors declare that they have no competing interests.

Special thank goes to Dennis Kiesler¹² for many helpful suggestions as well as his help with respect to SEM analyses and the manual annotation of the test samples.



The carbon dioxide, which was emitted due to the training of artificial neural networks for this publication was fully compensated on behalf of the lead author, by donating to *atmosfair gmbH*.^{13,14}

Acronyms

ANN	artificial neural network
CNN	convolutional neural network
COCO	common objects in context
CPU	central processing unit
DPN	DeepParticleNet
GPU	graphics processing unit
HT	Hough transformation
MAPE	mean absolute percentage error
PS	ParticleSizer
PSD	particle size distribution
ROI	region of interest
RPN	region proposal network
SEM	scanning electron microscopy
SGDM	stochastic gradient descent with momentum
synthPIC	synthetic particle image creator
TEM	transmission electron microscopy
UE	ultimate erosion
WST	watershed transformation

Symbols

A	area
α	learning rate
A_{convex}	convex area
α_{max}	maximum optimal learning rate
α_{min}	minimum optimal learning rate
AP	average precision
$\Delta d_{g,\%}$	percentage error of the geometric mean diameter
$\Delta N_{\%}$	percentage error of the number of primary particles
$\Delta \sigma_{g,\%}$	percentage error of the geometric standard deviation
$\Delta X_{\%,i}$	percentage error
d_{Feret}	Feret diameter
d_g	geometric mean diameter
D_{KL}	Kullback-Leibler divergence
i	index
IoU	intersection over union
$\mathcal{L}_{\text{training}}$	training loss
$\mathcal{L}_{\text{validation}}$	validation loss
MAPE	mean absolute percentage error
N	number of primary particles
n	number of dates
n_{training}	number of training samples
P	probability distribution
Q_i	probability distribution
S	solidity
σ	standard deviation
σ_g	geometric standard deviation
T_i	desired value
T_{sinter}	sintering temperature
X_i	actual value

¹²<https://orcid.org/0000-0002-2219-9773>

¹³<https://www.atmosfair.de/en/>

¹⁴Neither the authors nor the institutions they represent have any affiliation with *atmosfair gmbH*.

References

- [1] D. Schulze, Pulver und Schüttgüter: Fließigenschaften und Handhabung, 3rd Edition, VDI-Buch, Springer Berlin Heidelberg, Berlin, Heidelberg, 2014.
- [2] I. L. Schneider, E. C. Teixeira, L. F. Silva Oliveira, F. Wiegand, Atmospheric particle number concentration and size distribution in a traffic-impacted area, *Atmospheric Pollution Research* 6 (5) (2015) 877–885. doi:10.5094/APR.2015.097.
- [3] R. T. Rodrigues, J. Rubio, New basis for measuring the size distribution of bubbles, *Minerals Engineering* 16 (8) (2003) 757–765. doi:10.1016/S0892-6875(03)00181-X.
- [4] M. R. Azari, A. Yazdian, R. Zendehtel, H. Souri, S. Khodakarim, H. Peirovi, D. Panahi, M. Kazempour, Improved Method for Analysis of Airborne Asbestos Fibers Using Phase Contrast Microscopy and FTIR Spectrometry, *Tanaffos* 13 (3) (2014) 38–45.
- [5] J. Cheng, J. C. Rajapakse, Segmentation of clustered nuclei with shape markers and marking function, *IEEE transactions on bio-medical engineering* 56 (3) (2009) 741–748. doi:10.1109/TBME.2008.2008635.
- [6] C. Jung, C. Kim, Segmenting clustered nuclei using H-minima transform-based marker extraction and contour parameterization, *IEEE transactions on bio-medical engineering* 57 (10 PART 2) (2010) 2600–2604. doi:10.1109/TBME.2010.2060336.
- [7] J. Shu, H. Fu, G. Qiu, P. Kaye, M. Ilyas, Segmenting overlapping cell nuclei in digital histopathology images, in: 2013 35th annual international conference of the IEEE Engineering in Medicine and Biology Society (EMBC), IEEE, Piscataway, NJ, 2013, pp. 5445–5448. doi:10.1109/EMBC.2013.6610781.
- [8] C. Park, J. Z. Huang, J. X. Ji, Y. Ding, Segmentation, Inference and Classification of Partially Overlapping Nanoparticles, *IEEE transactions on pattern analysis and machine intelligence* 35 (3) (2013) 669–681. doi:10.1109/TPAMI.2012.163.
- [9] Z. Wang, A semi-automatic method for robust and efficient identification of neighboring muscle cells, *Pattern Recognition* 53 (2016) 300–312. doi:10.1016/j.patcog.2015.12.009.
- [10] F. E. Kruijs, J. van Denderen, H. Buurman, B. Scarlett, Characterization of Agglomerated and Aggregated Aerosol Particles Using Image Analysis, *Particle & Particle Systems Characterization* 11 (6) (1994) 426–435. doi:10.1002/ppsc.19940110605.
- [11] D. Ballard, Generalizing the Hough transform to detect arbitrary shapes, *Pattern Recognition* 13 (2) (1981) 111–122. doi:10.1016/0031-3203(81)90009-1.
- [12] P. M. Merlin, D. J. Farber, A Parallel Mechanism for Detecting Curves in Pictures, *IEEE Transactions on Computers* C-24 (1) (1975) 96–98. doi:10.1109/T-C.1975.224087.
- [13] L. Xu, E. Oja, P. Kultanen, A new curve detection method: Randomized Hough transform (RHT), *Pattern Recognition Letters* 11 (5) (1990) 331–338. doi:10.1016/0167-8655(90)90042-Z.
- [14] M. Frei, F. E. Kruijs, Fully automated primary particle size analysis of agglomerates on transmission electron microscopy images via artificial neural networks, *Powder Technology* 332 (2018) 120–130. doi:10.1016/j.powtec.2018.03.032.
- [15] E. Hamzeloo, M. Massinaei, N. Mehrshad, Estimation of particle size distribution on an industrial conveyor belt using image analysis and neural networks, *Powder Technology* 261 (2014) 185–190. doi:10.1016/j.powtec.2014.04.038.
- [16] Y.-D. Ko, H. Shang, A neural network-based soft sensor for particle size distribution using image analysis, *Powder Technology* 212 (2) (2011) 359–366. doi:10.1016/j.powtec.2011.06.013.
- [17] I. Goodfellow, Y. Bengio, A. Courville, Deep learning, *Adaptive computation and machine learning*, 2016.
- [18] A. Mehle, B. Likar, D. Tomažević, In-line recognition of agglomerated pharmaceutical pellets with density-based clustering and convolutional neural network, *IPSN Transactions on Computer Vision and Applications* 9 (1) (2017) 7. doi:10.1186/s41074-017-0019-2.
- [19] A. Heimowitz, J. Adán, A. Singer, APPLE Picker: Automatic Particle Picking, a Low-Effort Cryo-EM Framework. URL <http://arxiv.org/pdf/1802.00469v2>
- [20] D. Kriesel, A Brief Introduction to Neural Networks (2007). URL <http://www.dkriesel.com>
- [21] K. He, G. Gkioxari, P. Dollár, R. Girshick, Mask R-CNN. URL <http://arxiv.org/pdf/1703.06870v3>
- [22] R. C. González, R. E. Woods, S. L. Eddins, Digital image processing: Using MATLAB, Prentice Hall, Upper Saddle River, NJ, 2004.
- [23] H. Lee, R. Grosse, R. Ranganath, A. Y. Ng, Unsupervised learning of hierarchical representations with convolutional deep belief networks, *Communications of the ACM* 54 (10) (2011) 95. doi:10.1145/2001269.2001295.
- [24] L. Deng, Deep Learning: Methods and Applications, *FNT in Signal Processing (Foundations and Trends in Signal Processing)* 7 (3-4) (2013) 197–387. doi:10.1561/20000000039.
- [25] J. Hui, Image segmentation with Mask R-CNN (2018). URL https://medium.com/@jonathan_hui/image-segmentation-with-mask-r-cnn-ebe6d793272
- [26] F. Babick, L. Hillemann, M. Stintz, T. Dillenburger, M. Pitz, A. Hellmann, S. Antonyuk, S. Ripperger, F. J. T. Huber, S. Will, R. Wernet, M. Seipenbusch, M. Gensch, A. Weber, D. Kiesler, E. Kruijs, R. Friehmelt, B. Sachweh, Multiparameter Characterization of Aerosols, *Chemie Ingenieur Technik* 90 (7) (2018) 923–936. doi:10.1002/cite.201700094. URL <https://onlinelibrary.wiley.com/doi/pdf/10.1002/cite.201700094>
- [27] D. J. C. MacKay, Information theory, inference, and learning algorithms, 17th Edition, 2016.
- [28] W. Abdulla, Mask R-CNN for object detection and instance segmentation on Keras and TensorFlow (2017).
- [29] F. Chollet, et al., Keras (2015).
- [30] M. Abadi, A. Agarwal, P. Barham, E. Brevdo, Z. Chen, C. Citro, G. S. Corrado, A. Davis, J. Dean, M. Devin, S. Ghemawat, I. Goodfellow, A. Harp, G. Irving, M. Isard, Y. Jia, R. Jozefowicz, L. Kaiser, M. Kudlur, J. Levenberg, D. Mané, R. Monga, S. Moore, D. Murray, C. Olah, M. Schuster, J. Shlens, B. Steiner, I. Sutskever, K. Talwar, P. Tucker, V. Vanhoucke, V. Vasudevan, F. Viégas, O. Vinyals, P. Warden, M. Wattemberg, M. Wicke, Y. Yu, X. Zheng, TensorFlow: Large-Scale Machine Learning on Heterogeneous Systems (2015). URL <https://www.tensorflow.org/>
- [31] Python Software Foundation, Python 3.5.2. URL <http://www.python.org/>
- [32] K. He, X. Zhang, S. Ren, J. Sun, Deep Residual Learning for Image Recognition. URL <http://arxiv.org/pdf/1512.03385v1>
- [33] A. Canziani, A. Paszke, E. Culurciello, An Analysis of Deep Neural Network Models for Practical Applications. URL <http://arxiv.org/pdf/1605.07678v4>
- [34] O. Russakovsky, J. Deng, H. Su, J. Krause, S. Satheesh, S. Ma, Z. Huang, A. Karpathy, A. Khosla, M. Bernstein, A. C. Berg, L. Fei-Fei, ImageNet Large Scale Visual Recognition Challenge. URL <http://arxiv.org/pdf/1409.0575v3>
- [35] T.-Y. Lin, M. Maire, S. Belongie, L. Bourdev, R. Girshick, J. Hays, P. Perona, D. Ramanan, C. L. Zitnick, P. Dollár, Microsoft COCO: Common Objects in Context. URL <http://arxiv.org/pdf/1405.0312v3>
- [36] L. N. Smith, Cyclical Learning Rates for Training Neural Networks. URL <http://arxiv.org/pdf/1506.01186v6>
- [37] B. Kenstler, Cyclical Learning Rate (CLR) (2017).
- [38] MATLAB and Image Processing Toolbox: Function: imfindcircles (2018). URL <https://www.mathworks.com/help/images/ref/imfindcircles.html>
- [39] C. A. Schneider, W. S. Rasband, K. W. Eliceiri, NIH Image to ImageJ: 25 years of image analysis, *Nature methods* 9 (7) (2012) 671–675. doi:10.1038/nmeth.2089.
- [40] Thorsten Wagner, Jan Eglinger, Thorstenwagner/Ij-Particlesizer: V1.0.9 Snapshot Release (2017). doi:10.5281/zenodo.820296.
- [41] MATLAB and Image Processing Toolbox: Function: regionprops (2018). URL <https://www.mathworks.com/help/images/ref/regionprops.html>
- [42] COCO - Common Objects in Context: Metrics (2019). URL <http://cocodataset.org/#detection-eval>
- [43] R. J. Hyndman, A. B. Koehler, Another look at measures of forecast accuracy, *International Journal of Forecasting* 22 (4) (2006) 679–688. doi:10.1016/j.ijforecast.2006.03.001.
- [44] K. P. Murphy, Machine learning: A probabilistic perspective, *Adaptive computation and machine learning series*, 2012.

Appendix

Table A.1: Relevant hardware of the utilized GPU server.

Mainboard	Supermicro X11DPG-QT
CPU	2 x Intel Xeon Gold 5118
GPU	4 x NVIDIA GeForce RTX 2080 Ti
RAM	12 x 8 GB DDR4 PC2666 ECC reg.
SSD (OS)	Micron SSD 5100 PRO 960 GB, SATA
SSD (data)	Samsung SSD 960 EVO 1 TB, M.2

Table A.2: Relevant software of the utilized GPU server.

OS (host)	Ubuntu 18.04.2 LTS
OS (docker)	Ubuntu 16.04.5 LTS
Python (docker)	3.5.2
Tensorflow (docker)	1.13.1

Table A.3: Possible image augmentations.

Flip: left-right	50 %
Flip: up-down	50 %
Rotation	90°, 180° or 270°
Multiplication	0.8 to 1.5
Gaussian Blur	$\sigma = 0$ to 0.5

Table A.4: Final training conditions.

Backbone	ResNet-50
Initial Weights	COCO
Number of Training Samples	400
Number of Validation Samples	100
Image Augmentation	0 to 2 of Table A.3
Batch Size	4
Iterations per Epoch	100
Optimizer	SGDM [44]
Learning Rate Cycle Policy	triangular
Minimum Learning Rate	0.0005
Maximum Learning Rate	0.0037
Learning Rate Cycle Length	4 epochs
Momentum	0.9
Weight Decay	10^{-4}
Early Stopping Patience	20 epochs